# Supporting Information

# Hygroscopic Micro/Nanolenses along Carbon Nanotube Ion Channels

Yun-Tae Kim,[‡] Hyegi Min,[†] Michael S. Strano,[¶] Jae-Hee Han,[#,*] and Chang Young Lee[†,‡,*]

[†]School of Energy and Chemical Engineering, Ulsan National Institute of Science and Technology, Ulsan 44919, Republic of Korea

[‡]School of Life Sciences, Ulsan National Institute of Science and Technology, Ulsan 44919, Republic of Korea

[¶]Department of Chemical Engineering, Massachusetts Institute of Technology, Cambridge, Massachusetts 02139, United States

[#]Department of Materials Science and Engineering, Gachon University, Seongnam 13120, Republic of Korea

[*]E-mail: jhhan388@gachon.ac.kr, cylee@unist.ac.kr

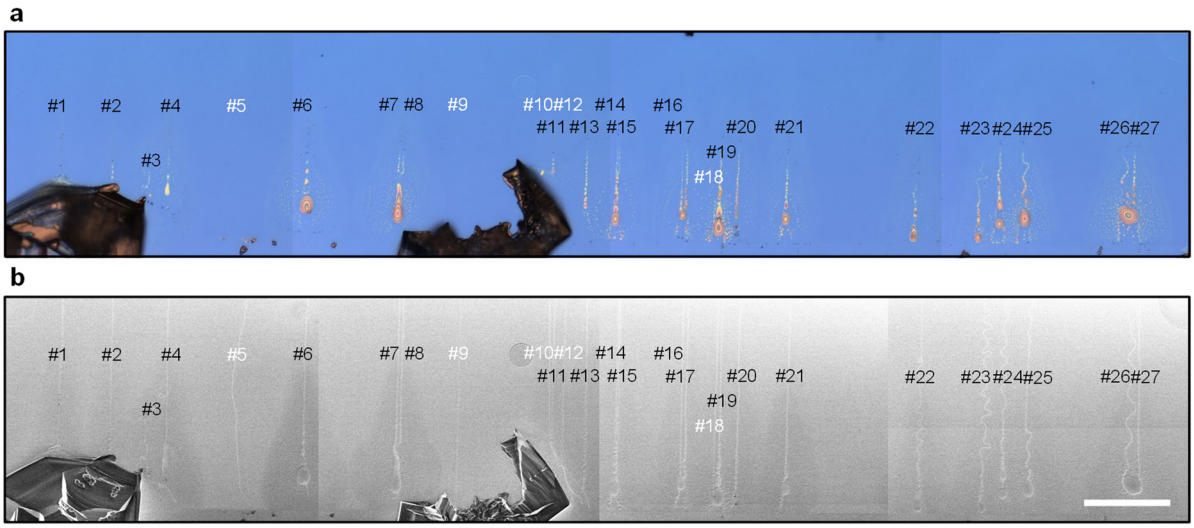


**Figure S1.** Optical visualization of the individual carbon nanotubes by salt crystals. (a) Optical image of the NaCl crystals formed along the nanotubes. (b) Corresponding SEM image of the NaCl crystals in (a), verifying that salt crystals were formed along almost all nanotubes. Among the 27 nanotubes, 22 could be optically visualized. Scale bar: 100 μm.

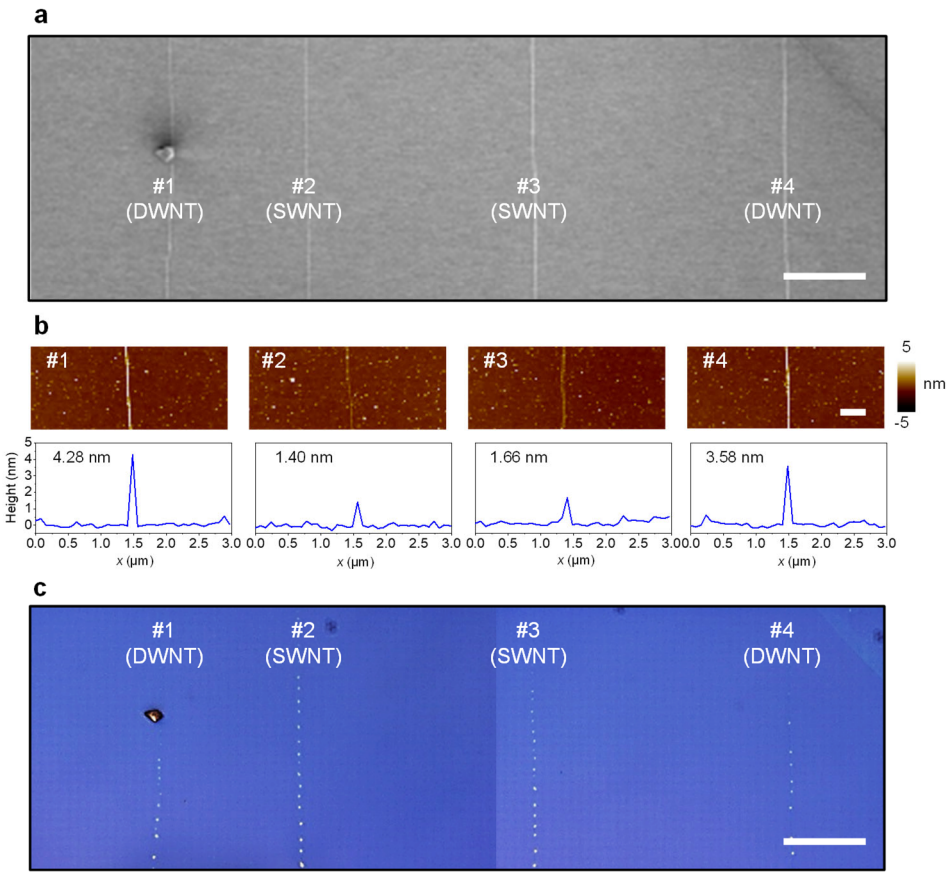


**Figure S2.** Formation of salt crystals along nanotubes with broad range of diameters. (a) SEM image of four nanotubes before being decorated with salt crystals. Scale bar: 20 μm. (b) AFM height images and corresponding height profile showing that nanotubes #1 and #4 were double-walled carbon nanotubes (DWNT) and that nanotubes #2 and #3 were single-walled nanotubes. Scale bar, 1 μm. (c) Optical image of salt crystals formed along all four nanotubes, suggesting that salt crystals were able to form on a wide range of carbon nanotubes. Scale bar: 20 μm.

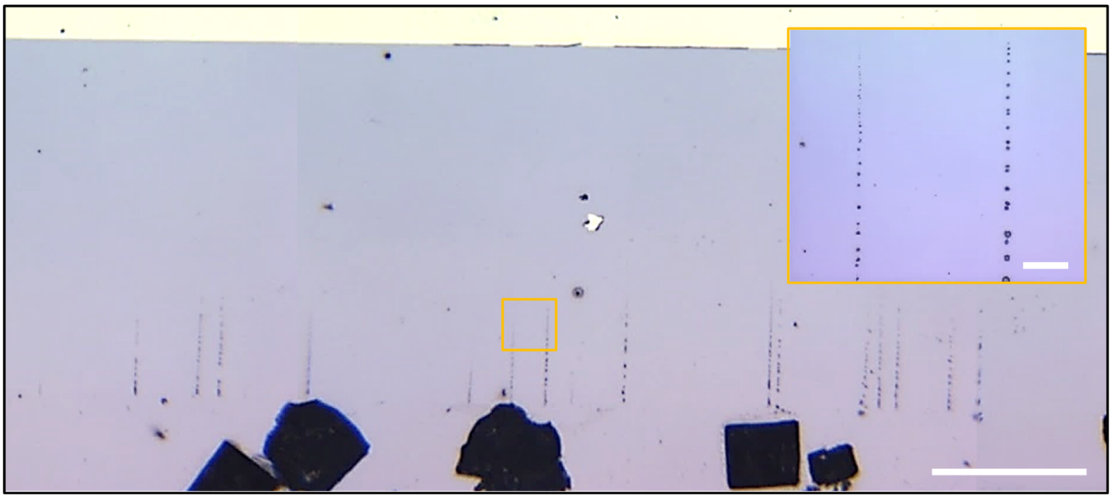

**Figure S3.** Formation of salt crystals along nanotubes on a bare silicon substrate. Imaging nanotubes on a highly-doped and conducting silicon substrate is difficult, but under an optical microscope the array of salt crystals help locate individual nanotubes. Scale bar: 300 µm. Inset shows a magnification of the area in the yellow box. Scale bar: 20 µm.

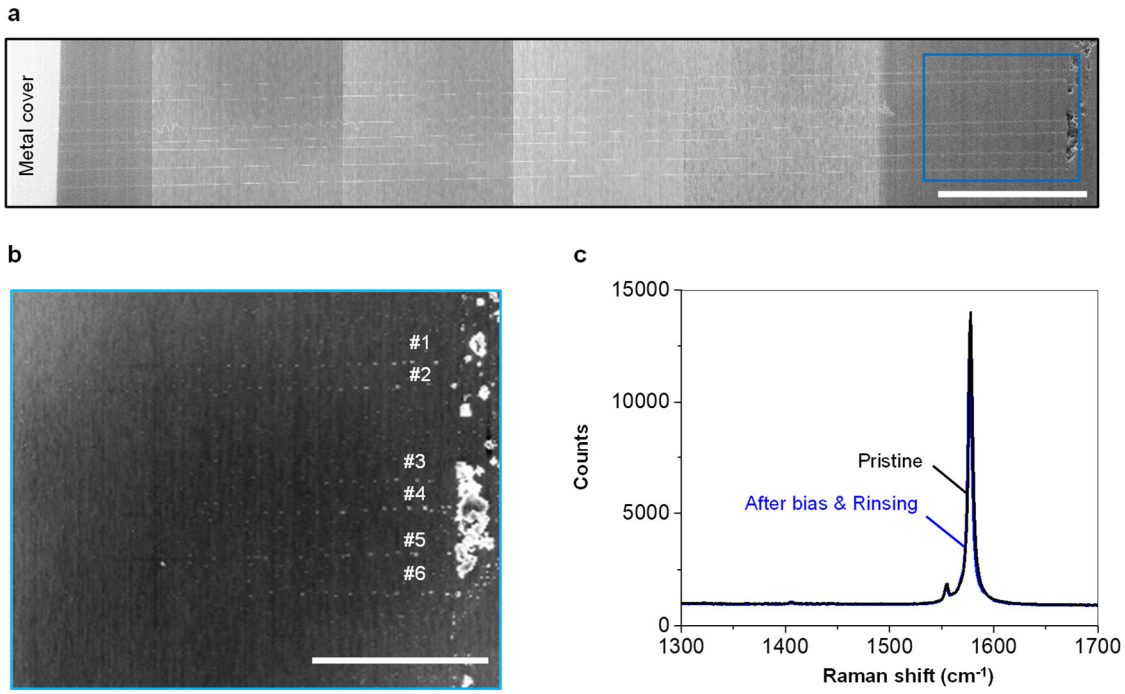


**Figure S4.** SEM and Raman spectra showing no damage to the nanotubes by the crystal formation. (a) SEM image of 1.3-mm long nanotubes after applying a 5 V electrical bias. No cut nanotubes were observed on either the metal cover or salt reservoir interfaces. Scale bar: 200 µm. (b) Magnified SEM image of the area in the blue box in (a), showing that all six nanotubes were able to form salt crystals (SEM acceleration voltage: 10 kV). Scale bar: 100 µm. (c) Raman spectra of SWNT before application of the bias (black) and after the bias and water rinsing (blue). No increase in the disorder mode (D-peak) suggested that the transport of the ionic solution was not damaging to the nanotubes.

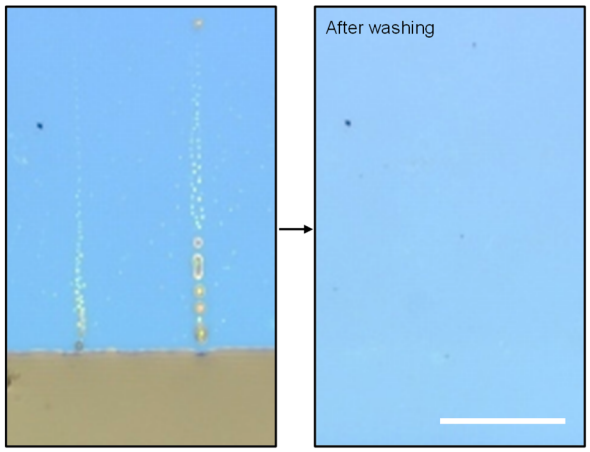


**Figure S5.** Removal of the salt crystals by simple rinsing with DI water: before (left) and after (right). Scale bar: 50 μm.

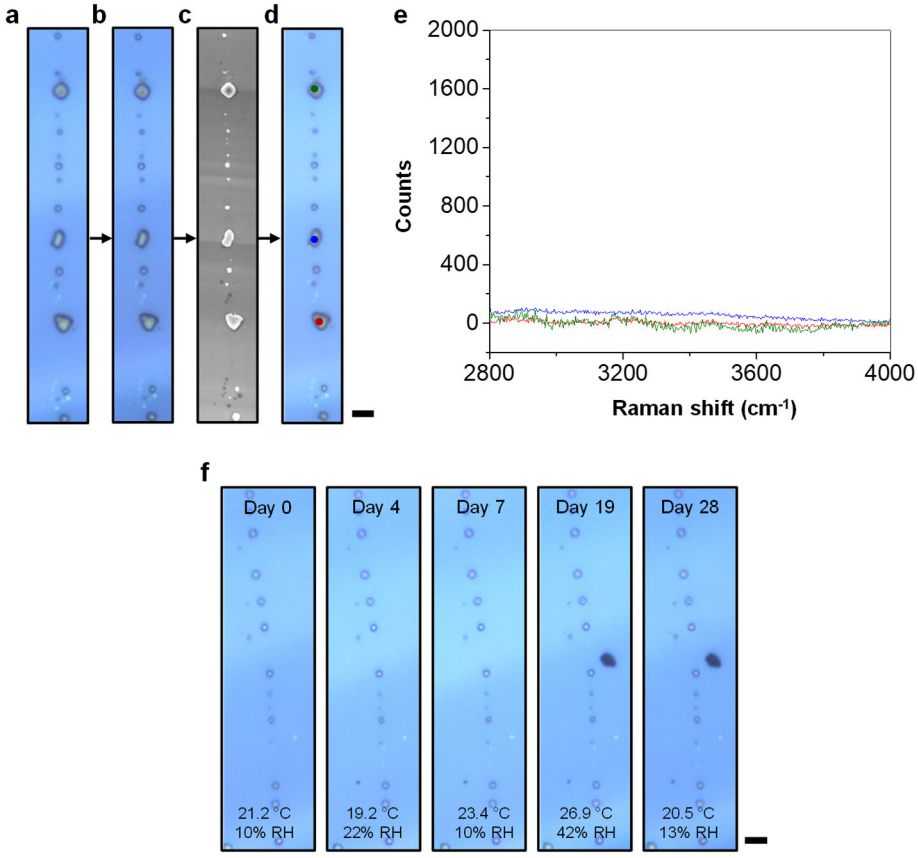


**Figure S6.** The robustness of the NaCl lenses. (a) Optical image of the NaCl lenses formed along a nanotube under ambient conditions (21.1 °C, 10% relative humidity). (b) Baking of the substrate at 100 °C for 2800 s; the shape and size of the lenses did not change. (c) SEM image of the same lens array. (d) Optical micrograph after taking the SEM image. The results of a-d show that the lenses were in the solid-state below the ERH of the salts, which is 45% for NaCl. Scale bars in a-d: 5 μm. (e) Raman spectra collected from the lens, showing no O-H stretching (3000–3600 $cm^{-1}$) under ambient condition (21.8 °C, 40% relative humidity). This result further confirmed that the lenses were in the solid-state below the ERH. (f) NaCl lenses on a SWNT stored under various ambient conditions (temperature 20–27 °C, relative humidity 10–42%) and observed for 28 days, verifying the stability of the lenses. Scale bar: 5 μm.

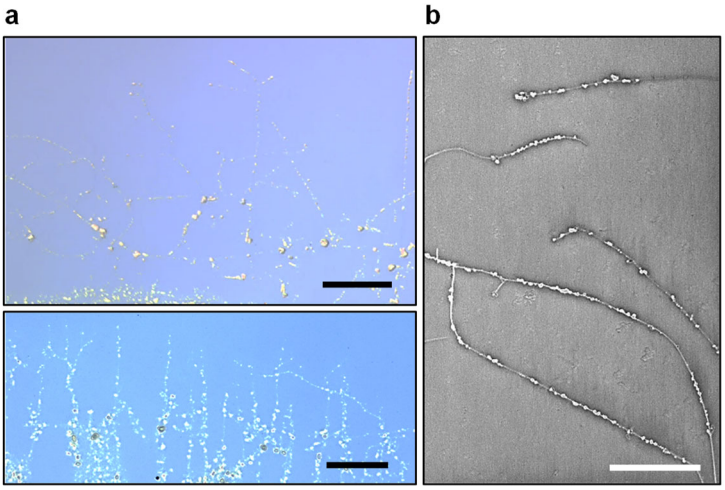


**Figure S7.** Formation of salt micro/nanostructures on a random network of SWNTs. (a) Optical images of NaCl micro/nanostructures formed along the random networks of SWNTs after application of a bias. Scale bars, 20 μm (top) and 50 μm (bottom). (b) SEM images of NaCl micro/nanostructures formed along random networks of SWNTs. Scale bar, 5 μm.

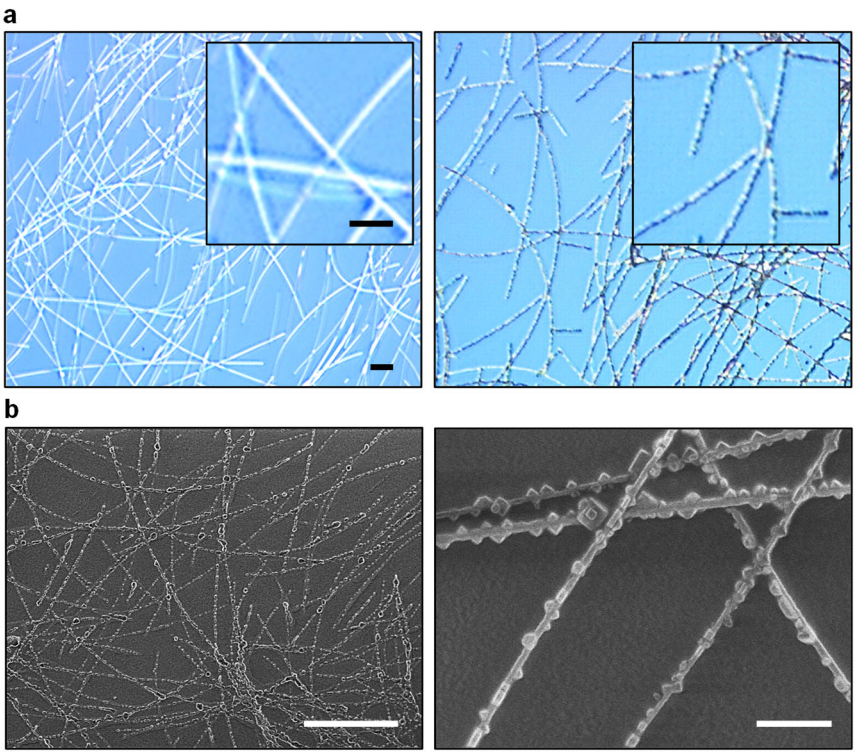


**Figure S8.** Formation of salt structures on a random network of silver nanowires. (a) Optical images of NaCl micro/nanostructures formed along the random networks of silver nanowires (d = 115 nm) before (left) and after applying bias (right). Inset shows magnified images. Scale bars, 5 μm. (b) SEM images of NaCl micro/nanostructures formed along random networks of silver nanowires. Scale bars, 20 μm (left) and 1 μm (right).

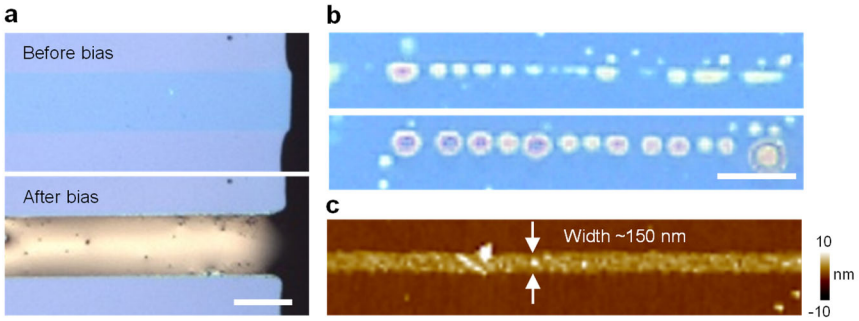


**Figure S9.** Formation of salt structures on graphene ribbons. (a) Optical images of a graphene microribbon (width 100 μm) before (top) and after (bottom) applying bias. Liquid film of NaCl was formed along the graphene microribbon. Scale bar, 100 μm. (b) Optical images of NaCl microstructures formed along graphene nanoribbons (width ~150 nm) after application of a bias. Scale bar, 20 μm. (c) AFM image of a graphene nanoribbon, showing width of ~ 150 nm.

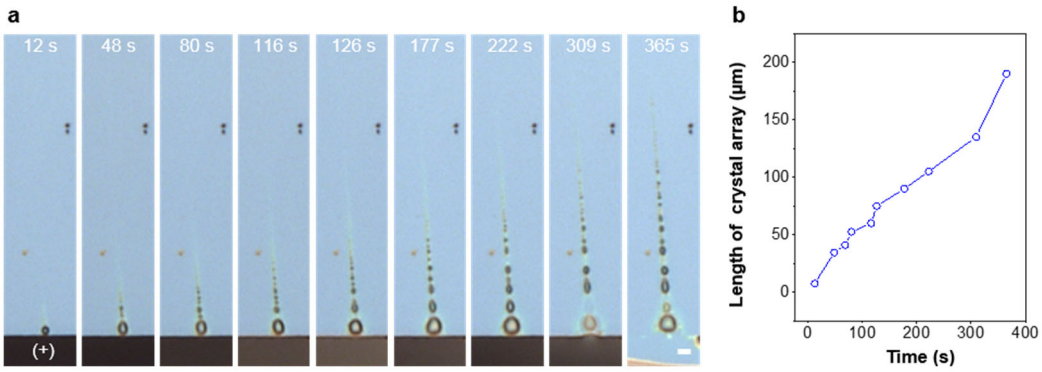


**Figure S10.** *In situ* monitoring of the formation of micro/nanocrystals of NaCl. (a) Formation of salt crystals along a SWNT by ionic transport under ambient condition (23.2 °C, 60% relative humidity). Scale bar: 10 μm. (b) Length of the array of salt crystals versus time. The length of array continued to increase with time.

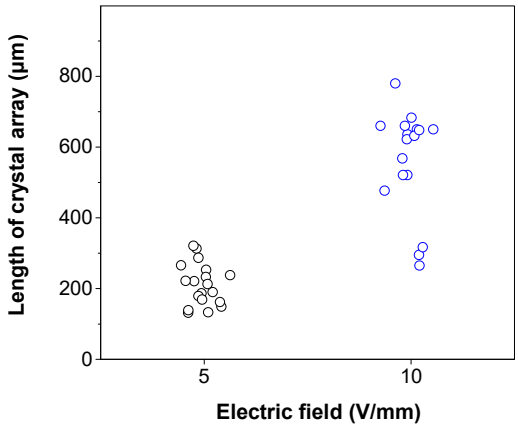


**Figure S11.** Length of the array of NaCl crystals as function of the electric field. The ionic transport time was fixed at 400 s.

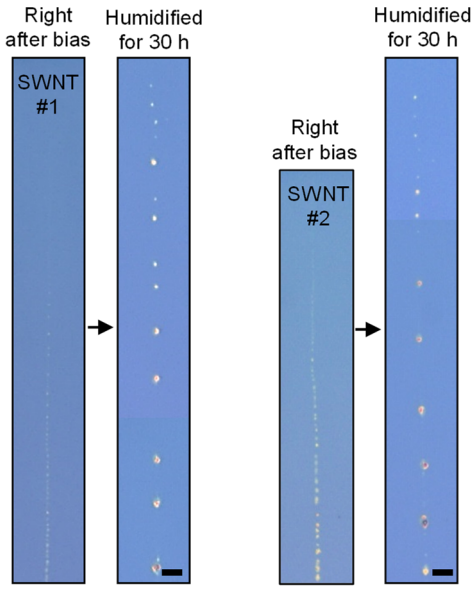


**Figure S12.** Increasing the size and distance between the lenses at higher relative humidity. Optical images of NaCl micro/nanostructures formed along two SWNTs (#1 and #2) right after bias (left) and after storage in humidified conditions (96% RH) for 30 h (right). Scale bars, 10 μm.

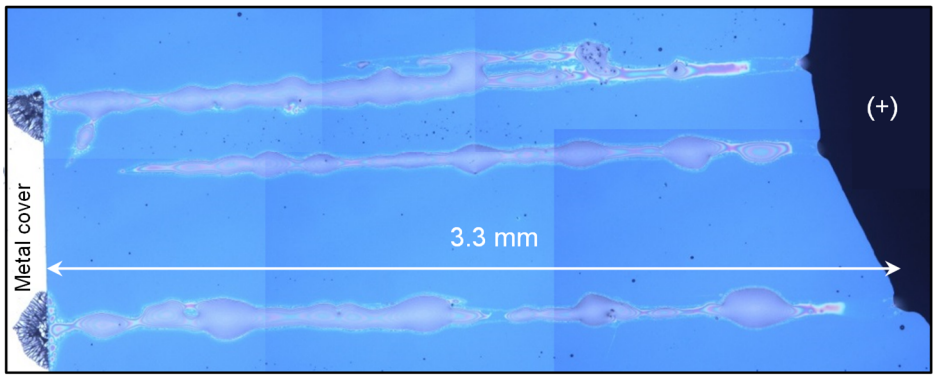


**Figure S13.** Optical image of the NaCl liquid formed along the nanotubes under ambient condition (25.2 °C, 70% relative humidity). An electrical bias of 40 V was applied between the metal cover and 3M NaCl solution for 3 min. In this case, oxygen plasma etching was not performed.

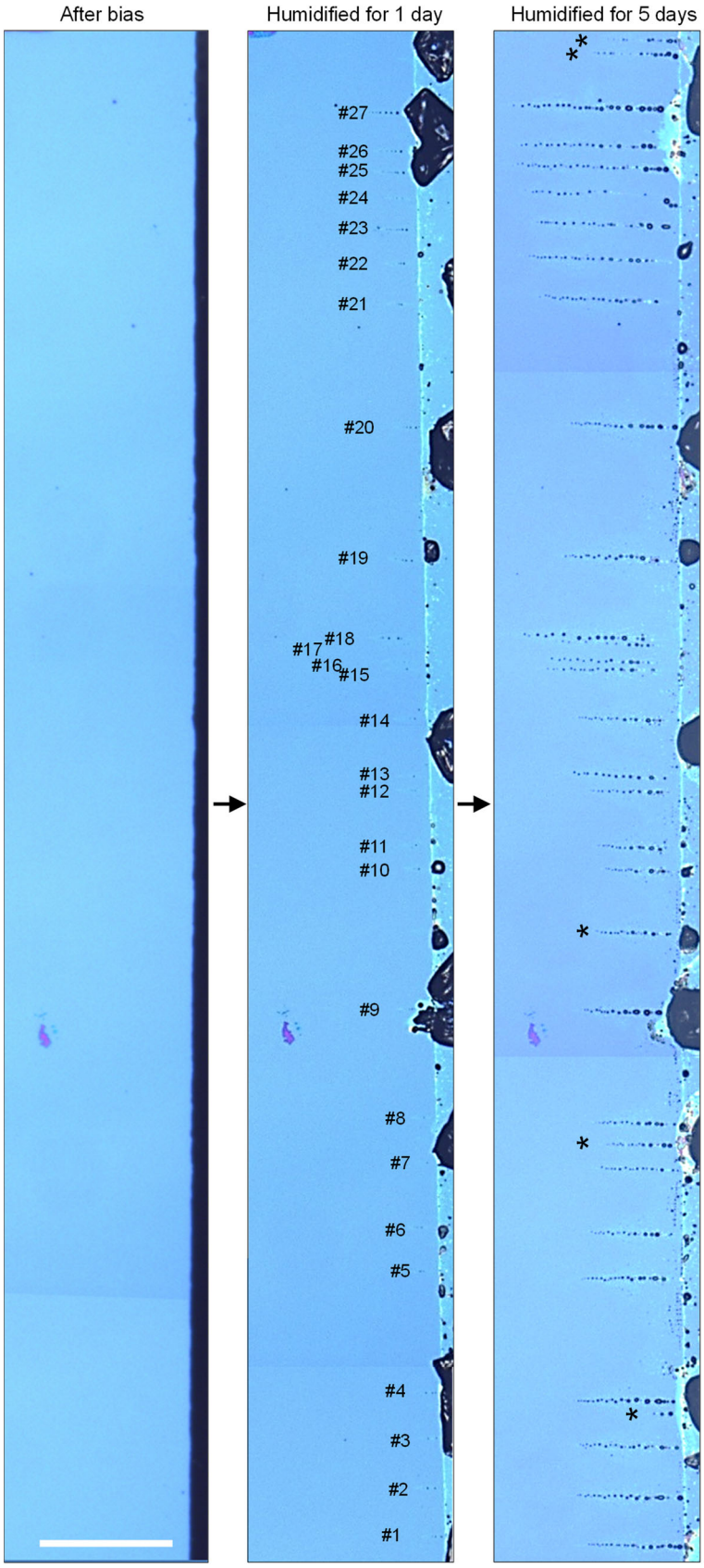


**Figure S14.** A sample after the transport of 0.16 M KI (left) by applying 40 V/mm for 1 min, stored in humidified condition for 1 day (middle) and 5 days (right) without applying bias. Asterisks indicate nanotubes that were not visible on day 1 but became visible on day 5. Scale bar: 300 μm

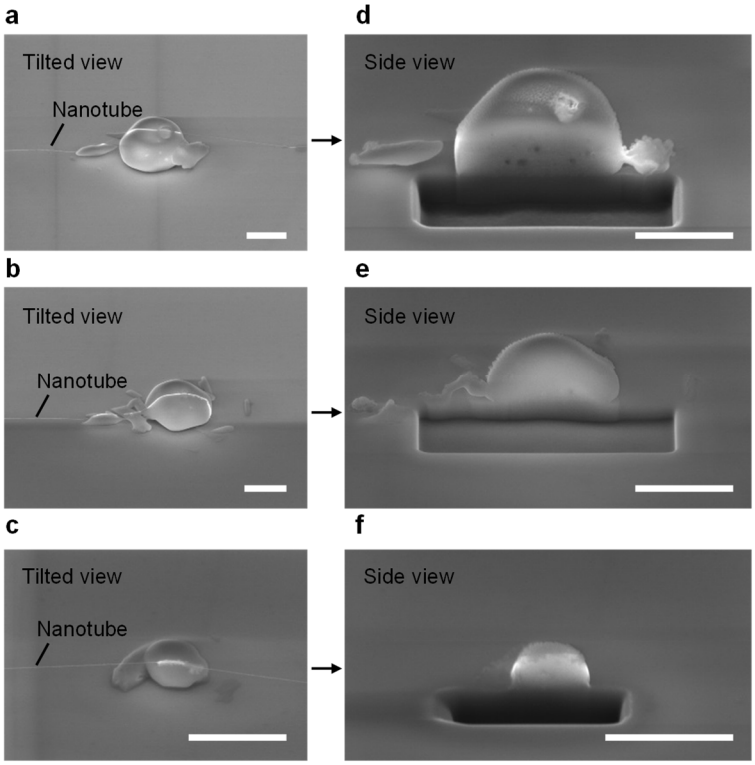


**Figure S15.** The plano-convex shape of the NaCl crystal lenses. (a-c) Tilted-view SEM images of NaCl lenses. (d-f) Side-view SEM images of the lenses in a-c, half-cut using a focused ion beam, showing the plano-convex shape. All scale bars: 1 μm.

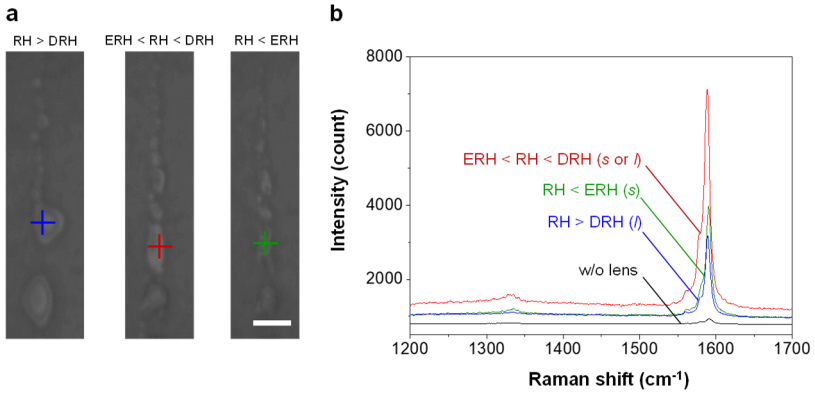


**Figure S16.** Raman enhancement of a SWNT by salt structures under different humidity conditions. (a) Optical images of NaCl micro/nanostructures formed along a nanotube under different relative humidity values. Scale bar, 5 μm. (b) Raman spectra of salt microstructures formed along nanotube under different relative humidity, demonstrating a large enhancement regardless of the phase of the lens.

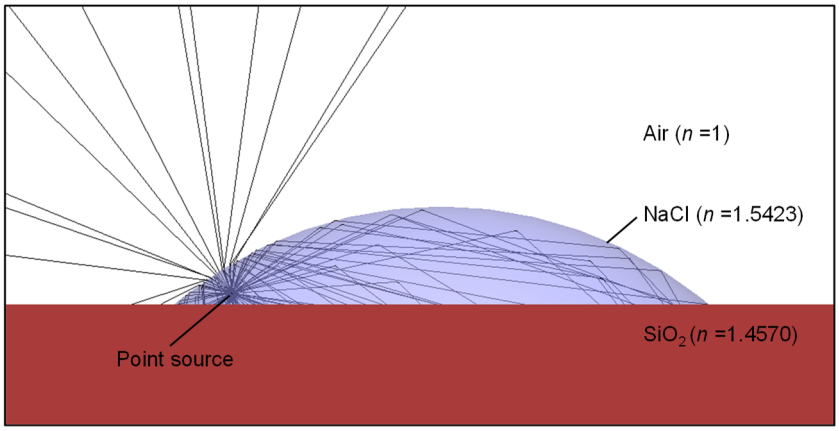


**Figure S17.** A ray-tracing simulation showing total internal reflection of within the lens. Ray optics simulation was conducted by LightTools software with a point source of light (λ = 633 nm) placed near the edge of a NaCl lens ($d$ = 1 μm, $n$ = 1.5423) on a 300 nm thick $SiO_2$ layer ($n$ = 1.4570).

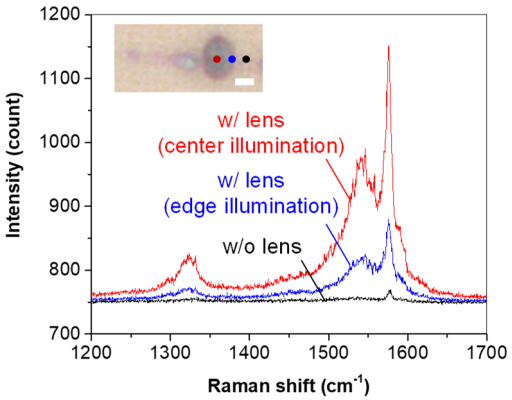


**Figure S18.** Raman spectra of a SWNT from three different spots near a microlens: without the lens (black), near the edge of the lens (blue), and at the center of the lens (red), as indicated in optical micrograph of NaCl lenses on the nanotube (inset). Raman spectra were obtained at 633 nm excitation. Scale bar, 1 μm.

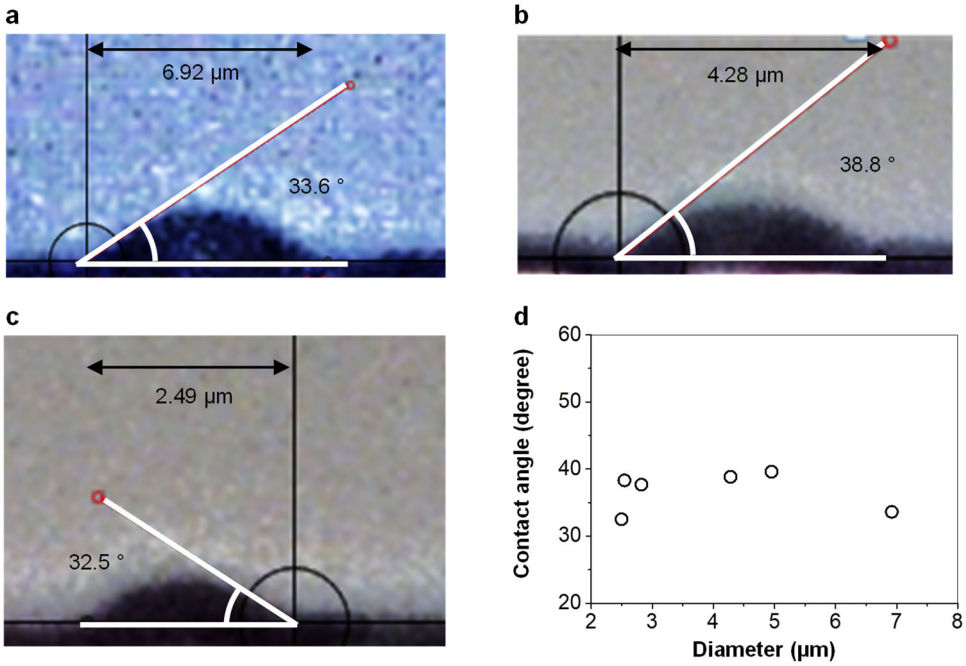


**Figure S19.** Contact angles of the microlenses. (a-c) Optical images of three different lenses with diameters of 6.92, 4.28, and 2.49 μm on a silicon substrate. The lenses were formed by transitioning salt crystals to liquid droplets under ambient conditions (22.9 °C and 65% relative humidity). (d) Contact angles measured from the microlenses. Based on these results, we chose 40° as the contact angle used for the FDTD calculation.

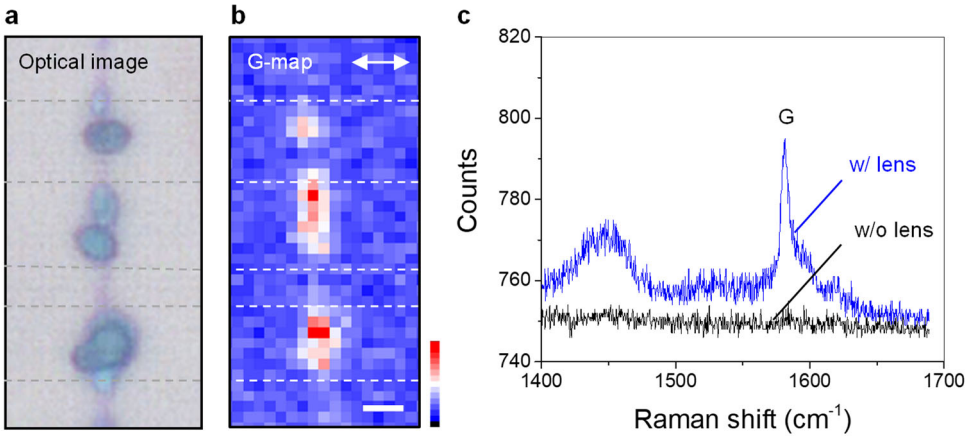


**Figure S20.** Enhanced Raman scattering of SWNT excited with a polarized laser. (a) Optical image of NaCl microlenses formed on a SWNT. (b) G-map collected with an excitation laser (λ = 633 nm) polarized perpendicular to the SWNT axis. Scale bar, 2 μm. (c) Raman spectra from the lens (w/ lens, blue) and the bare nanotube between lenses (w/o lens, black), showing the G-peak only in the presence of the lens.

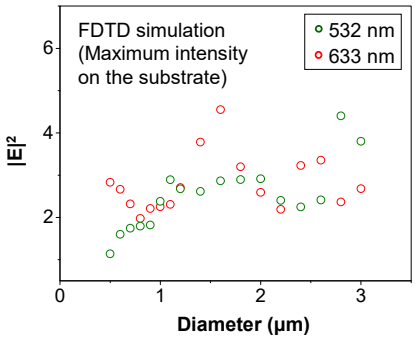


**Figure S21.** FDTD simulation showing maximum intensity on the substrate at the center of the lens, plotted versus the lens diameter upon excitation at 532 nm (green) and 633 nm (red).

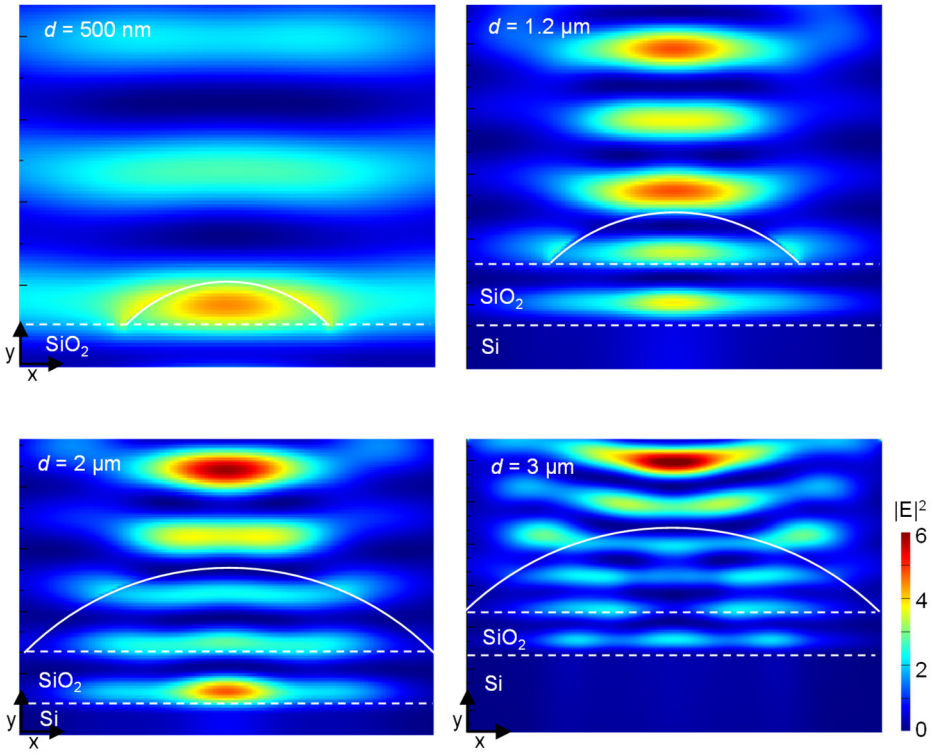


**Figure S22.** Dependence of electromagnetic wave on the lens diameter. FDTD simulation was performed on micro/nanolenses ($n$ = 1.33, contact angle = 40°) with different diameters (0.5, 1.2, 2 and 3 μm) on $SiO_2$/Si substrate illuminated by a plane wave at 633 nm. In small lenses, with diameter close to the wavelength of the light, the intensity maximum was located within the lens. In larger lenses, however, the maxima were located outside the lens. The results can be attributed to near-field focusing behavior of subwavelength-size lenses.[1]

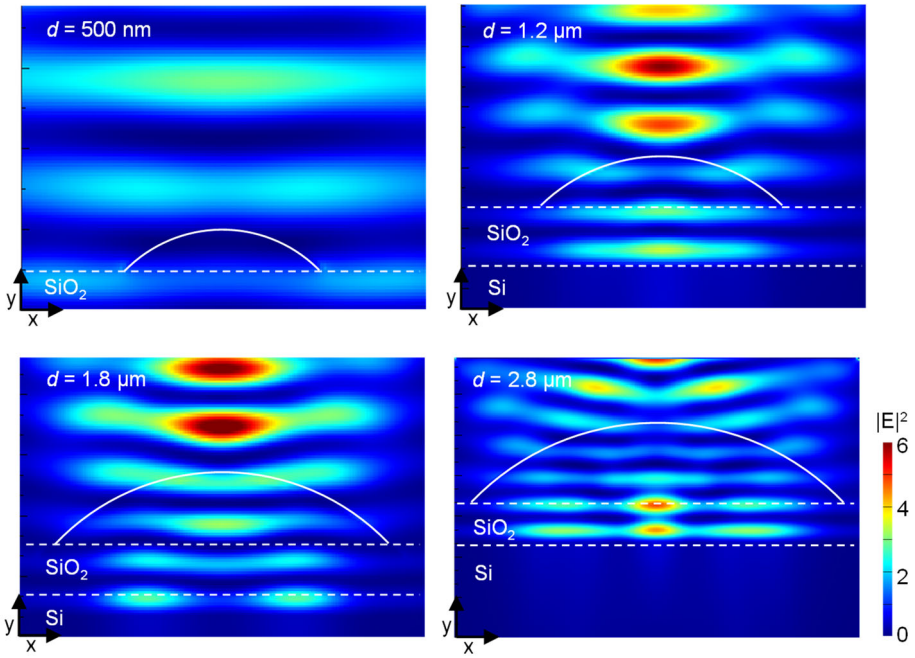


**Figure S23.** Dependence of electromagnetic wave on the lens diameter. FDTD simulation was performed on micro/nanolenses (n = 1.33, contact angle = 40°) with different diameters (0.5, 1.2, 1.8 and 2.8 μm) on SiO2/Si substrate illuminated by a plane wave at 532 nm. Maximum intensity within the lens increases with the lens diameter, showing the opposite trend with FDTD results of 633 nm.

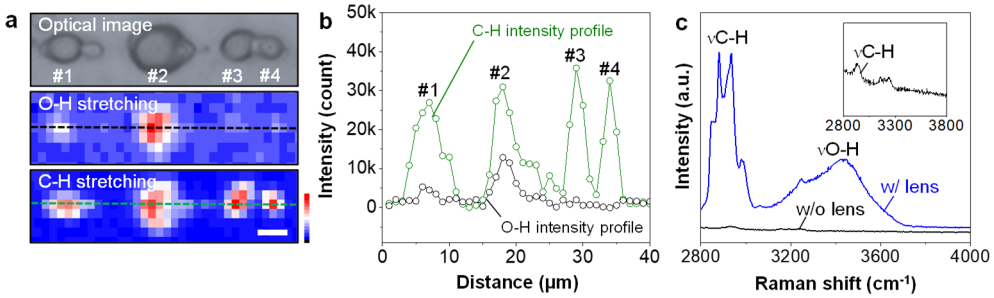


**Figure S24.** Detection of carbonaceous species on a SWNT. (a) Optical image and Raman map of NaCl microdroplets on a SWNT under humidified conditions with the droplets numbered from #1 through #4. Scale bar, 2 μm. (b) Intensity profile of dashed line in a. Lenses #3 and #4 show strong intensity of C-H stretching but no O-H stretching, indicating that the enhancement is achieved by the lens and not by the aqueous environment. (c) The corresponding spectra with (blue) and without (black) the lens under 532 nm excitation, showing the stretching modes of the O-H (3000-3600 $cm^{-1}$) of water and the C-H (2800-3000 $cm^{-1}$) of amorphous carbon on the nanotube. Without the lens, only weak C-H stretching was observed (inset), whereas strong O-H and C-H stretching modes were detected with the lens. Here, the O-H stretching mode of water confirmed that the lenses were aqueous microdroplets of the NaCl solution. The C-H stretching mode suggested the presence of carbonaceous species on the nanotube, which may have been deposited either during the synthesis of the nanotube or via electron-beam-induced deposition during SEM imaging.[2]

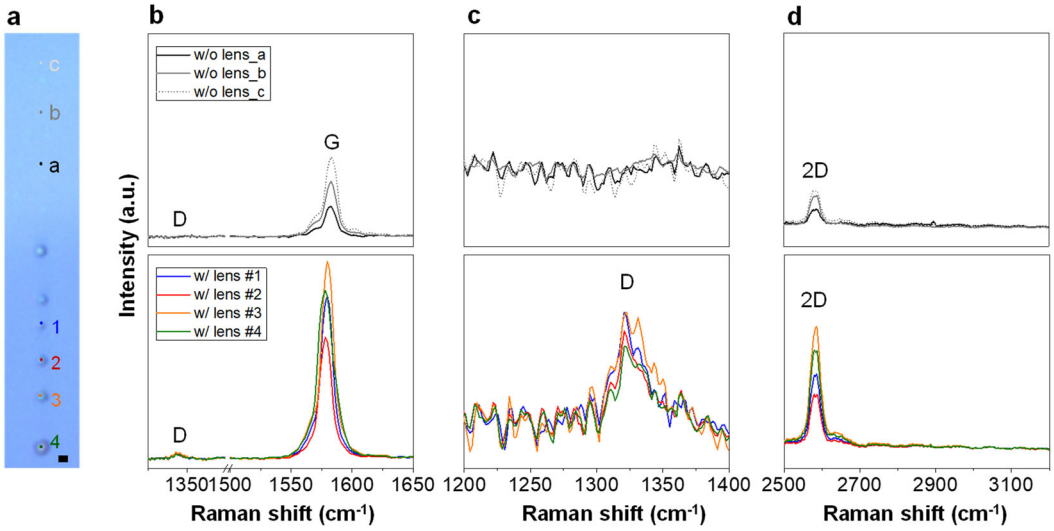


**Figure S25.** Amplified Raman spectra of a lightly functionalized SWNT by salt lenses. We performed on-chip chemistry[3] in which the nanotube was treated with a 10 μM solution of 4-bromobenzene diazonium tetrafluoroborate in 0.1 mM NaOH for 10 min. After an array of NaCl lenses was formed by ionic transport, Raman spectra were collected from the functionalized nanotube. (a) Optical image of NaCl lenses along a SWNT lightly functionalized with 4-bromobenzene diazonium. Labelled along the SWNT are the spots without lenses (a through c) and the ones with lenses (1 through 4). Scale bar: 1 μm. (b) Raman spectra of the SWNT from the spots labelled in (a), without (top) and with (bottom) the lenses, collected under 633 nm excitation and a relative humidity of 41%. (c) The enlarged D-mode (~1320 $cm^{-1}$) in (b), a signature of covalent chemistry, is detectable only with the lens. (d) The spectra in (b) shown in the higher wavenumber range. The enhancement occurred in every Raman mode of the SWNT. The absence of the O-H stretching (3000-3600 $cm^{-1}$) verified that the lenses were in the solid-state. The absence of C-H stretching (2800-3000 $cm^{-1}$) confirmed that the increased D-mode originated from the diazonium chemistry and not from residual amorphous carbon.

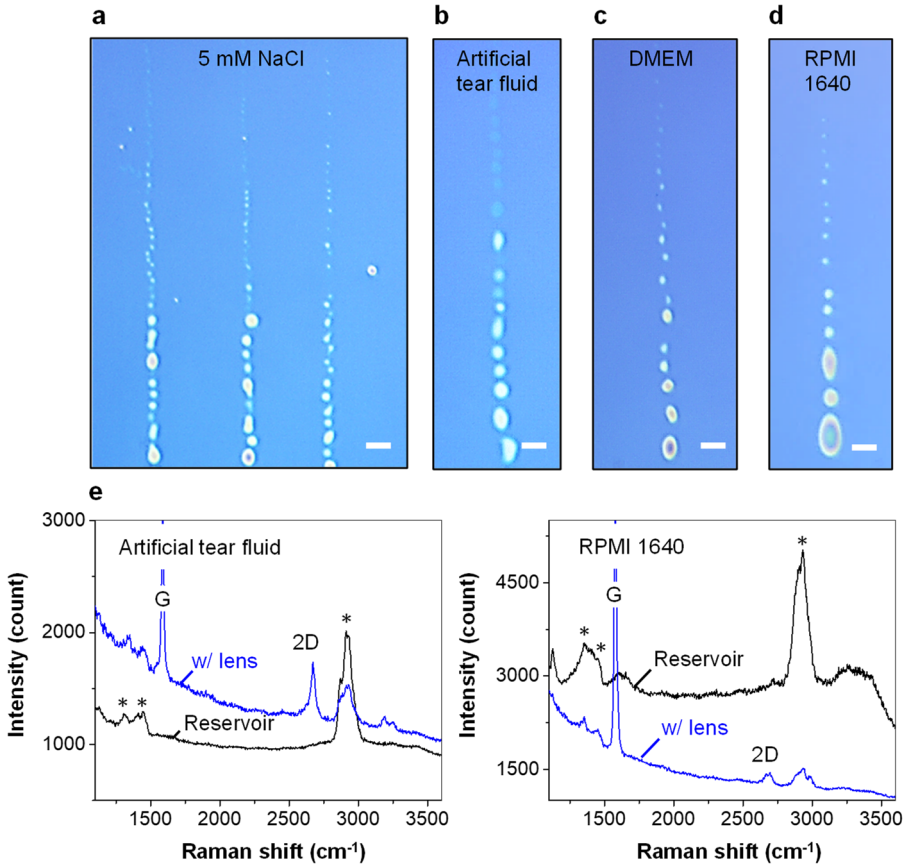


**Figure S26.** Formation of micro/nanolenses on SWNTs using various ionic species. (a-d) Optical images of micro/nanolenses formed by transporting (a) NaCl solution at 5 mM, (b) artificial tear fluid, and mammalian cell culture media (c) DMEM (Dulbecco's Modified Eagle Medium) and (d) RPMI (Roswell Park Memorial Institute) 1640. Scale bars, 5 µm. (e) Raman spectra of artificial tear fluid (left) and cell culture media (right, RPMI 1640), collected from the microlens formed along the nanotube at 52% RH. Characteristic Raman modes are marked with asterisks.

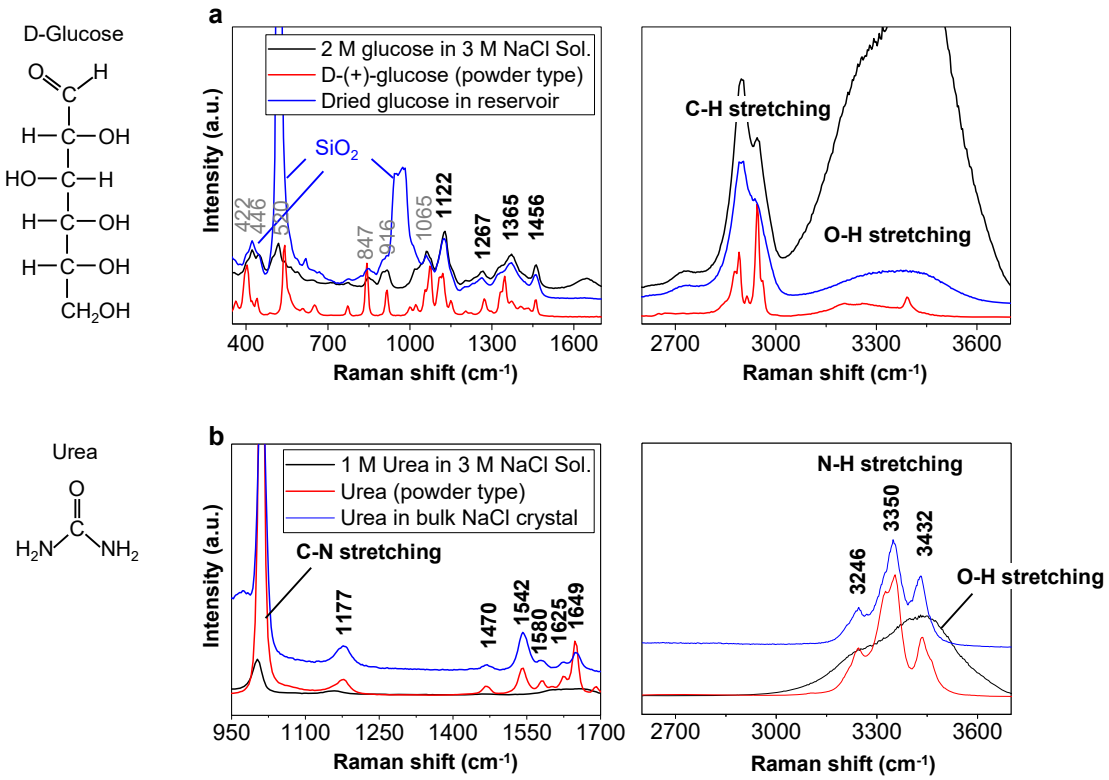


**Figure S27.** Fingerprints of Raman-active molecules. (a) Raman spectra of different states of glucose (bulk aqueous state, powder, and captured in an NaCl crystal).[4] The 12 Raman modes at 442, 446, 520, 847, 916, 1065, 1122, 1267, 1365, 1456, C-H stretching (2800-3000), and O-H stretching (3000-3600 $cm^{-1}$) are considered the Raman fingerprint of glucose. The O-H stretching of the microlens and reservoir originate from glucose, not from water, as the humidity (41%) was lower than the ERH of NaCl (45%). Among the 12 fingerprint Raman modes, only 6 modes (1122, 1267, 1365, 1456 $cm^{-1}$, C-H, and O-H stretching) were detectable due to overlap with the $SiO_2$ background. (b) Raman spectra of different states of urea (bulk aqueous state, powder, and captured in an NaCl crystal).[5] The nine Raman modes at 1177, 1470, 1542, 1580, 1625, 1649, and the N-H stretching (3246, 3350, 3432) are considered the Raman fingerprint of urea. Among the nine Raman fingerprint modes, those related to N-H stretching (3246, 3350, 3432) were clearly distinguishable within the Raman scattering range of the nanotube.

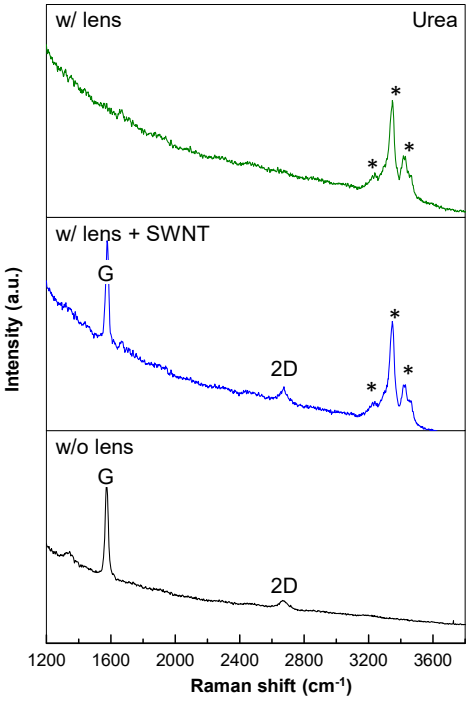


**Figure S28.** Raman spectra of a SWNT and urea from different locations. Raman spectra after transport of urea collected from a NaCl lens on the nanotube, showing only the urea peaks (top, w/ lens), both the urea peaks and the SWNT peaks (middle, w/lens + SWNT), and the SWNT peaks only (bottom, w/o lens). The spectrum at the bottom was collected from bare SWNT without the lens. Characteristic Raman modes of glucose or urea are marked with asterisks.

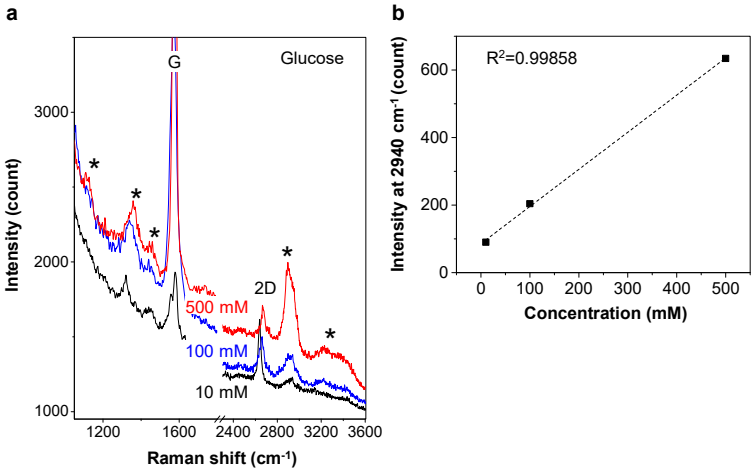


**Figure S29.** Detection of glucose at low concentrations using salt microlenses. (a) Raman spectra after the transport of glucose with different concentrations, collected from NaCl microlenses on a nanotube. Here the diameters of NaCl lens are 4.1 (500 mM), 3.8 (100 mM) and 3.8 μm (10 mM), respectively. Characteristic Raman modes of glucose are marked with asterisks. (b) Raman intensity at 2940 $cm^{-1}$ as a function of glucose concentrations.

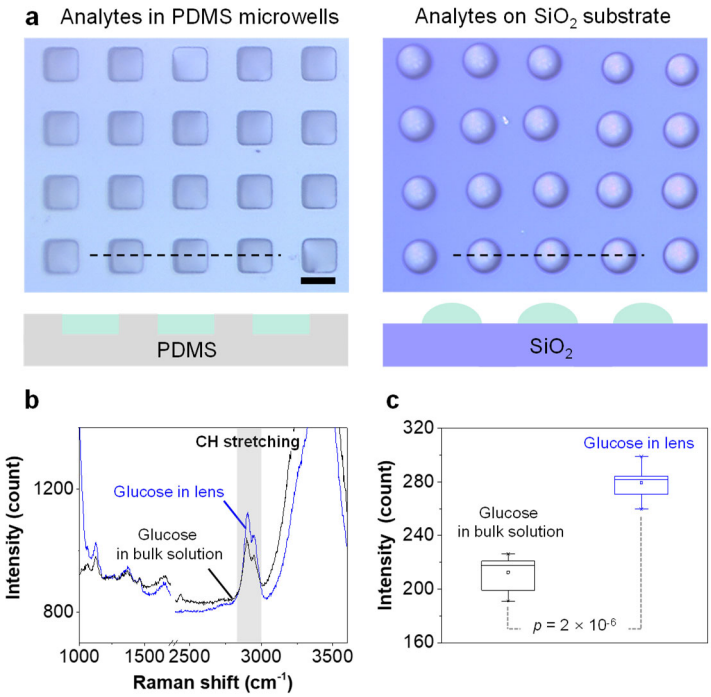


**Figure S30.** Enhanced Raman scattering by plano-convex lenses. (a) Optical micrographs of PDMS microwells (10 μm × 10 μm × 5 μm) filled with 0.5 M glucose solution in 3 M LiCl (left), and microlenses of the glucose solution transferred from the microwells onto a $SiO_2$/Si substrate (right). Shown at the bottom illustrates cross-sectional view along the dotted line in each micrograph. Scale bar, 10 μm. (b) Raman spectra from the glucose in microlens (blue) and in bulk droplet (black). (c) Intensity of the C-H stretching of glucose (2800 – 3000 $cm^{-1}$) in microlenses (blue) and in bulk droplet (black), obtained from 10 spectra for each. All Raman spectra were obtained at 532 nm excitation and relative humidity of 55%.

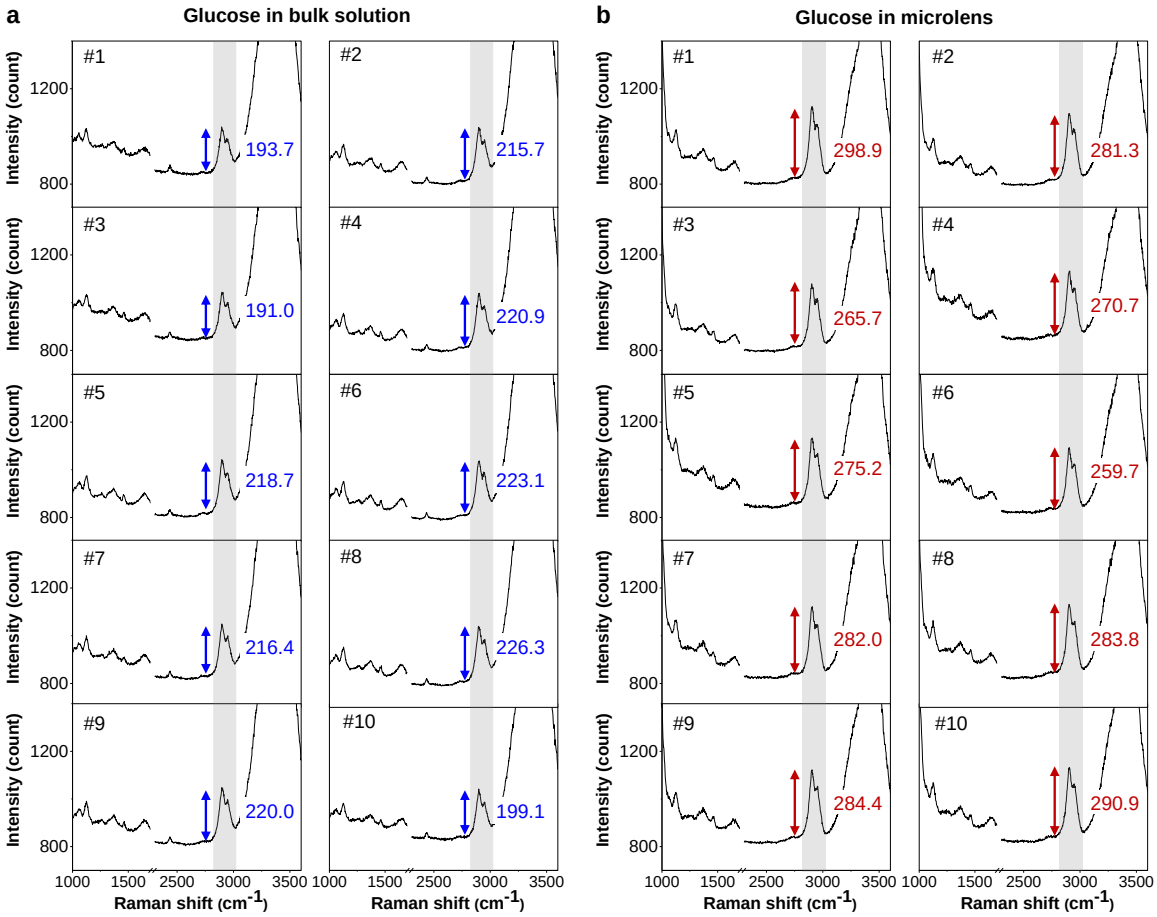


**Figure S31.** Raman spectra used to create Figure S30c, obtained from glucose (a) in microlenses and (b) in a bulk droplet, with the C-H stretching at 2800 – 3000 $cm^{-1}$ shaded in grey.

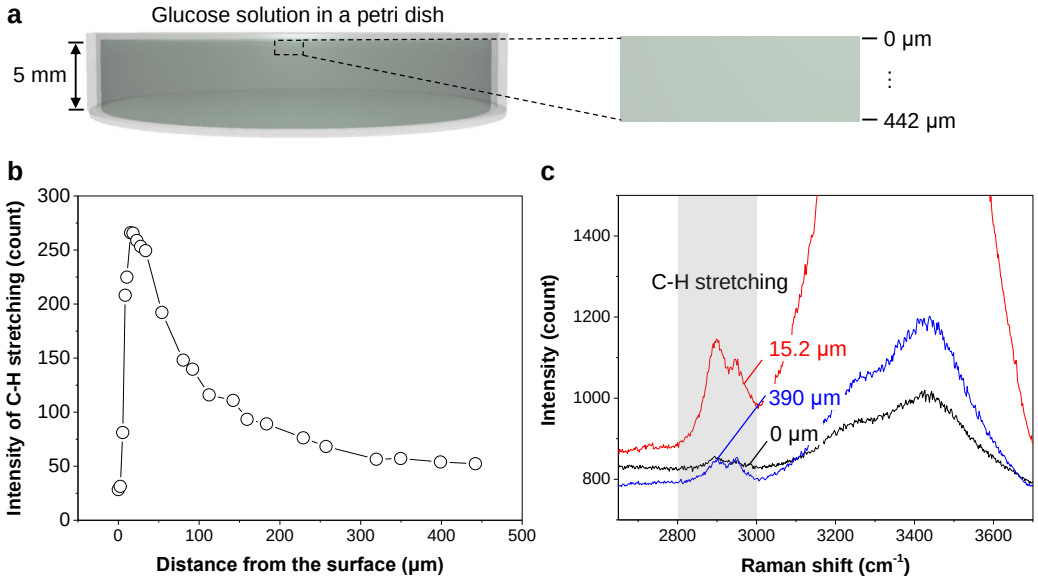


**Figure S32.** Depth-dependent Raman scattering of glucose in a bulk solution. (a) Schematic illustration showing depth profiling of a 5 mm-deep solution of glucose in a petri dish. (b) Intensity of C-H stretching (2800-3000 $cm^{-1}$) plotted versus the depth of focal plane from the air-solution interface. The glucose concentration was 0.5 M in 3 M LiCl solution, and the spectra were collected at 532 nm excitation and relative humidity of 53%. (c) Raman spectra of glucose at depths of 0, 15.2, and 390 μm.

## References

(1) Lee, J. Y.; Hong, B. H.; Kim, W. Y.; Min, S. K.; Kim, Y.; Jouravlev, M. V.; Bose, R.; Kim, K. S.; Hwang, I. C.; Kaufman, L. J.; Wong, C. W.; Kim, P.; Kim, K. S., Near-field focusing and magnification through self-assembled nanoscale spherical lenses. *Nature* 2009, 460, 498-501.
(2) Choi, J. H.; Lee, J.; Moon, S. M.; Kim, Y.-T.; Park, H.; Lee, C. Y., A Low-Energy Electron Beam Does Not Damage Single-Walled Carbon Nanotubes and Graphene. *The Journal of Physical Chemistry Letters* 2016, 7, 4739-4743.
(3) Wang, C. J.; Cao, Q.; Ozel, T.; Gaur, A.; Rogers, J. A.; Shim, M., Electronically selective chemical functionalization of carbon nanotubes: Correlation between Raman spectral and electrical responses. *Journal of the American Chemical Society* 2005, 127, 11460-11468.
(4) Chattopadhyay, S.; Li, M. S.; Roy, P. K.; Wu, C. T., Non-enzymatic glucose sensing by enhanced Raman spectroscopy on flexible 'as-grown' CVD graphene. *Analyst* 2015, 140, 3935-3941.
(5) Frost, R. L.; Kristof, J.; Rintoul, L.; Kloprogge, J. T., Raman spectroscopy of urea and urea-intercalated kaolinites at 77 K. *Spectrochim Acta A* 2000, 56, 1681-1691.